

FEDSM2018-83091

VALIDATION STUDY OF COMPACT PLANING HULLS AT PRE-PLANING SPEEDS

Miles P. Wheeler

Washington State University
Pullman, WA, USA

Konstantin I. Matveev

Washington State University
Pullman, WA, USA

Tao Xing

University of Idaho
Moscow, ID, USA

ABSTRACT

Planing hard-chine hulls are often employed on fast boats to ensure high lift and moderate drag in high-speed regimes. Although such boats are usually designed for relatively light loadings, occasionally they may need to operate in overloaded conditions with reduced speed. The focus of this study is on planing hull hydrodynamics in such pre-planing, high-lift regimes. A numerical tool based on a finite-volume viscous solver is applied to simulate a compact planing hull in a speed range from the displacement to planing modes. Numerical results for the model-scale hull resistance, trim and sinkage are compared with experimental data. Additionally, an overloaded condition of this hull is simulated. The resulting variations of hydrodynamic parameters are discussed.

INTRODUCTION

A planing mode of fast boats is characterized by a dominant hydrodynamic lifting force, while the hydrostatic support becomes less important. Hulls intended for such regimes are usually designed with hard chines, such as experimentally studied by Fridsma [1]. Their design loadings are relatively light in comparison with typical loadings of displacement-type ships to ensure moderate drag at high speeds. However, in some circumstances, such as rescue missions, planing boats may have to operate in overloaded conditions. Due to higher resistance and increased weight, speeds achievable by heavy loaded boats will likely belong to pre-planing regimes.

Prediction methods for planing hull hydrodynamics have a long history. A number of simplified correlations were developed about 50 years ago, with Savitsky's equations being the most known and still commonly used [2]. These correlations however are not always sufficiently accurate, since they have simple forms and cover a very broad operational range. The linearized potential-flow methods were also developed in the past for simple planing forms [3,4] and were extended to account for more complicated features, e.g., stepped hulls and catamarans [5,6]. The potential-flow methods

are also useful due to their fast calculation times. With the advance of computational fluid dynamics (CFD) methods and computer power, it is now possible to simulate complex flows where viscous, nonlinear and other effects are accounted for. Examples of such studies can be found in previous works [7-9], where modeling efforts for the same model-scale hull were described. It should be noted that applications of CFD tools in marine hydrodynamics, while being already very popular, require significant computational resources and user knowledge and experience in both hull hydrodynamics and numerical modeling.

In the present study, we carried out numerical modeling of high-lift hulls in a speed range from the displacement to planing regimes, with a focus to predict the hump speed and drag. The CFD tool, STAR-CCM+, commonly used in marine hydrodynamics, is employed here as a finite-volume viscous solver to simulate flow around planing hulls. A compact planing hull with a relatively high loading is selected from available experimental literature for validation purpose [1]. In addition, an even heavier condition of the same hull is simulated, and the resulting changes in hydrodynamics of such an overloaded hull are discussed.

SOLVER AND MESHER SETTINGS

The geometry employed in this study corresponded to the prismatic hull used with the Fridsma experiment [1], with a length to beam ratio equal to 4 and 20-degree deadrise (Fig. 1). The chosen nominal weight had a beam loading coefficient of 0.608, with the beam coefficient defined as $\Delta/(wb^3)$, where Δ is the ship weight displacement, w is the specific weight of water, and b is the beam or maximum width of the hull. In the experiment, a piece of tape was added at the chines to help prevent hull wetting at intermediate speeds. Geometry was created to include this tape in the simulations.

The finite-volume CFD program used in this study was STAR-CCM+ v12.04.011. The Dynamic Fluid Body Interaction (DFBI) model was activated, and the hull was free to pitch and heave while subjected to a constant incoming flow. The

segregated flow solver with SIMPLE solution algorithm with second-order convection terms was used. A first-order implicit unsteady analysis was performed until the time-averaged flow characteristics stopped evolving. The Eulerian multi-phase approach employed constant density and viscosity for both the air and water, corresponding to fresh water properties used in the experiment reported by Fridsma [1]. The volume-of-fluid (VOF) method with the high-resolution interface capturing (HRIC) scheme served as the free surface interface capturing technique. The Reynolds Averaged Navier-Stokes (RANS) Realizable K-Epsilon Two Layer All Y+ turbulence solver was used. The governing equations include the continuity, momentum and volume fraction transport equations,

$$(1) \nabla \cdot \bar{\mathbf{v}} = 0 ,$$

$$(2) \frac{\partial}{\partial t}(\rho \bar{\mathbf{v}}) + \nabla \cdot (\rho \bar{\mathbf{v}} \otimes \bar{\mathbf{v}}) = -\nabla \cdot (\bar{p} \mathbf{I}) + \nabla \cdot (\mathbf{T} + \mathbf{T}_t) + \mathbf{f}_b ,$$

$$(3) \frac{\partial c}{\partial t} + \nabla \cdot (c \bar{\mathbf{v}}) = 0 ,$$

where \mathbf{v} is the flow velocity, ρ is the mixture density, p is the pressure, \mathbf{I} is the identity tensor, \mathbf{T} is the viscous stress tensor, \mathbf{T}_t is the Reynolds stress tensor, \mathbf{f}_b is the body force (such as gravity), and c represents the volume fraction occupied by air, so that the effective fluid density ρ and viscosity μ are calculated as $\rho = \rho_{air}c + \rho_{water}(1 - c)$ and $\mu = \mu_{air}c + \mu_{water}(1 - c)$. The overbar indicates flow properties with excluded turbulent fluctuations.

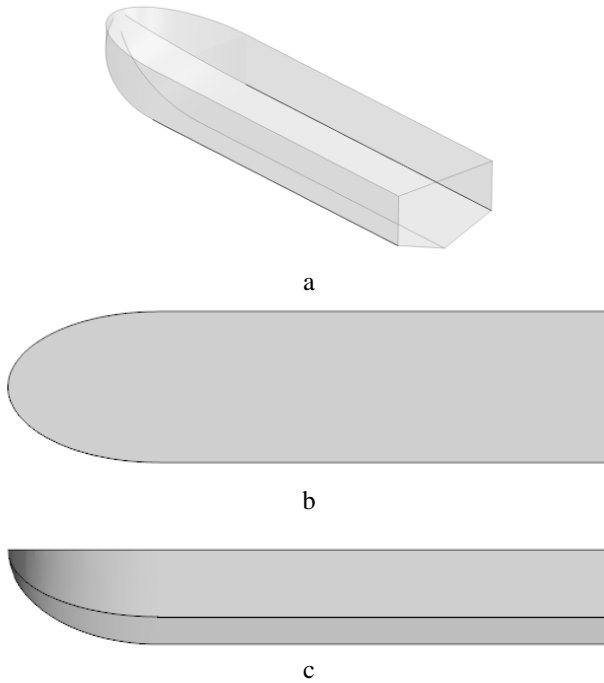


Fig. 1 Images of the hull geometry. a) 3D view; b) top view; c) side view.

In simulations the surface averaged Y+ values for the wetted hull surfaces in the models were kept below 5 for all models simulated here. The time step was equivalent to $L/(200 U)$, where L is the hull length and U is the velocity of the incident flow. A pseudo-transient method was used, in which the transient solver was used until steady state conditions were reached. Five inner iterations were performed on each time step during the simulations.

The boundary conditions assigned on all sides of the domain (except for the downstream boundary and symmetry plane) corresponded to the velocity inlets with the constant horizontal velocity, whereas the downstream boundary was treated as the pressure outlet. Symmetry was assumed, and only half model was simulated. The symmetry plane was placed along one side of the domain. The no-slip condition was used on the hull surface. An illustration of the boundary conditions can be seen in Fig. 2. The VOF-wave forcing zones of one ship length were used near the sides, upstream, and downstream boundaries. The initial conditions comprised the undisturbed water and air flows with the constant velocity reported in the experiments.

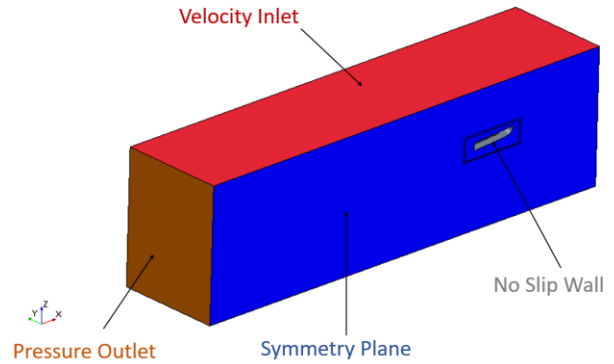


Fig. 2 Overview of boundary conditions. All unseen faces of the domain are velocity inlets.

The computational grid was generated in STAR-CCM+ v12.04.011, and an overset methodology with two overlapping regions was applied. The larger region, or background mesh, was composed of octree formed hexahedral cells with appropriate refinements added to capture the free surface and generated wave patterns. The overset region used a trimmed mesh with 15 prism layers. The overset interface employed a linear interpolation scheme between the background the overset grid. The background domain size is shown Fig. 3. The overset region and dimensions can be seen in Figs. 3 and 4. The mesh details near the strip on the hull chine are given in Fig. 4. The surface mesh on the hull is depicted in Fig. 5. The total number of cells used in the final simulations was 1.27 million.

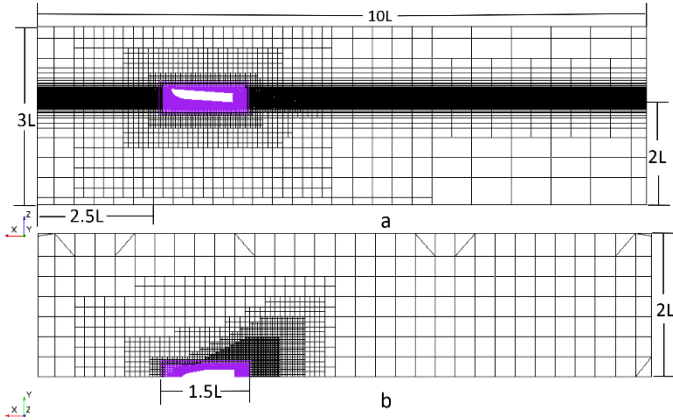


Fig. 3 Images of the mesh and domain. a) side view b) bottom view. Refinement zones can be seen and dimensions are listed. The background mesh is in black and the overset region is shown in purple.

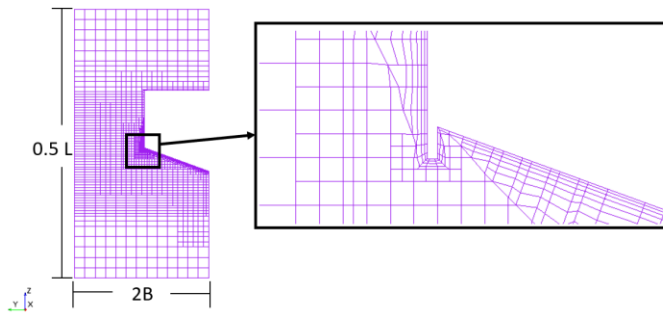


Fig. 4 Left, a cross-section near prismatic portion of the hull with height and width dimensions of the overset region. Right, zoomed-in view of the mesh near the protruding piece of tape.

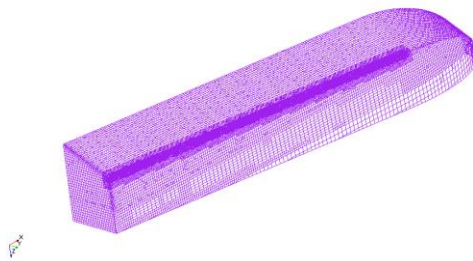


Fig. 5 Mesh at the surface of the hull. The bottom, starboard and rear sides of the hull are shown. The mesh refinements in the chine area envelop the protruding piece of tape.

Due to the hull curvature and high aspect ratio cells used to capture the appropriate Y^+ in the bow region, it was observed that air propagated down the hull in the near wall cells in areas we expected to be fully wetted. This phenomenon is often referred to numerical ventilation and is considered to be unphysical on hulls with sufficiently steep hull curvature [10]. The standard way to alleviate this issue is to add mesh

refinements in the areas where ventilation occurs in order to get better aspect ratio cells near the surface and stagnation points on the hull. In this study, it was observed that the mesh count would need to be increased on the order of at least 8 times to get rid of the numerical diffusion error. In order to save computational effort, an assumption was made that this heavy hull with sufficient trim was fully wetted, and the sink term for air fraction was added to the VOF solver. The model was first run without any additional sink term applied to get an idea of the wetted profile. Then, all the near-wall cells that had a volume fraction of water greater than 0.6 were identified. In these cells, a sink term to the air phase of VOF solver was applied to force the ventilated cells have water only. This sink term is then turned on for the rest of the simulation and the simulation is re-converged. A similar method was also used by Frisk and Tegehall [11].

A volume fraction of 0.6 was chosen here as the threshold to guarantee fully wetted surface while minimizing the amount of cells in which the source term was active. A sensitivity study was done with respect to the threshold level. The results obtained with several threshold values, as well as no sink term for reference, are shown in Fig. 6. It can be seen that there is virtually no difference between using thresholds of 0.6 and 0.4, and once the filter is above 0.6, significant ventilation is observed. With this approach, a coarser mesh can be used, and a reasonable agreement compared to the other studies can still be obtained. It should be noted that this approach would not be valid if physical ventilation was expected on the hull.

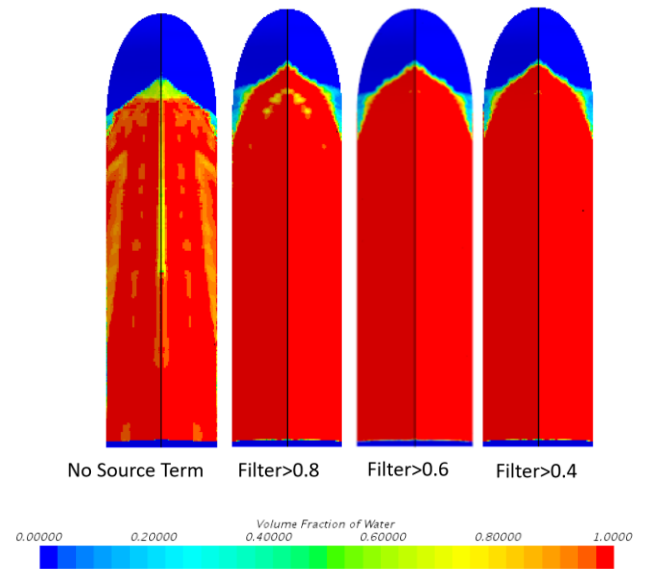


Fig. 6 Comparison of water volume fraction with and without the source term.

MESH-DEPENDENCY STUDY

In order to determine the numerical uncertainty associated with the grid and time step size, a systematic study was performed where the mesh was refined and the time step was decreased until acceptable grid convergence was achieved. The mesh ratio for the simulations was $\sqrt{2}$, and the corresponding time step was decreased by a factor of $\sqrt{2}$.

The resistance, trim, and heave were the critical responses investigated. The resistance is defined as the total force acting in the longitudinal direction parallel to the nominal water surface. The resistance is reported in a non-dimensional form, R/Δ , by normalizing the resistance force by the weight of the hull. Trim τ is defined as the rotational displacement about a transverse axis centered at the center of gravity of the hull and is reported here as the angle measured in degrees between the keel line of the hull and the nominal water surface. Positive values of trim indicate the bow has moved up. The heave h is defined as the vertical movement of the center of gravity compared to the hull at rest. Positive values indicate the center of gravity has moved upwards, and this parameter is also reported in a non-dimensional form, h/B , which normalizes the heave by the beam of the hull. These motions are illustrated in Fig. 7.

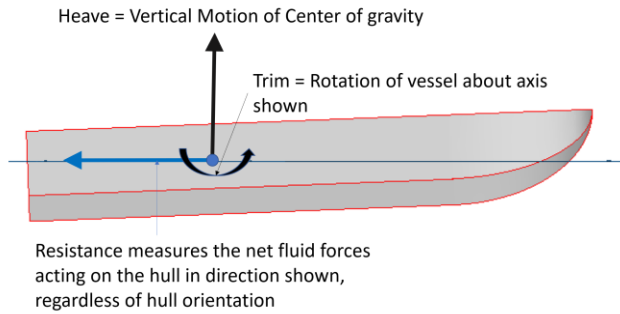


Fig. 7 Resistance, trim, and heave definitions.

Three different simulations were run in the mesh dependency study: coarse, medium, and fine grids were simulated at $Fr = 1.19$ and their results were compared. This speed was one of the more difficult for simulation speeds as it was close to the hump speed. The results for the different mesh levels are plotted in Fig. 8. Monotonic grid convergence was achieved, and an uncertainty analysis using the factors of safety for the Richardson extrapolation presented by Xing and Stern [12] was performed to determine the uncertainty in the grids. It was observed that the uncertainty in resistance was 5.2%, the uncertainty in trim was 1.5%, and the uncertainty in the heave was 8.7%. This is acceptable for engineering applications, and the finest grid size was then chosen and used for the rest of the simulations. The final mesh count was 1.27 million cells.

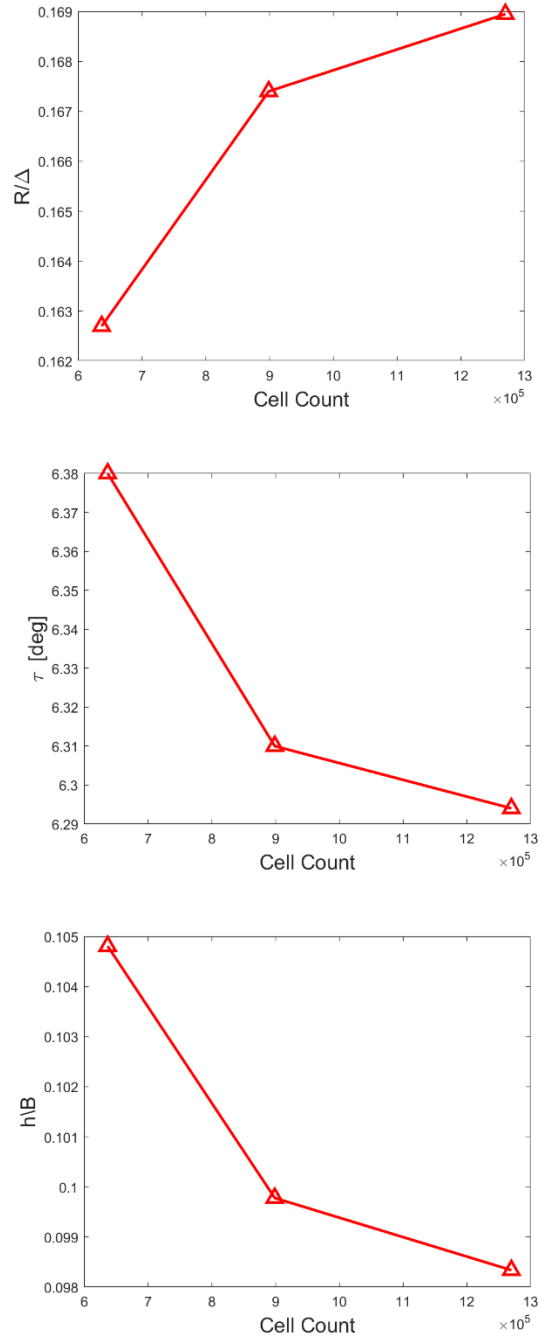


Fig. 8 Plots showing the mesh count effects on the response variables of interest: resistance to displacement ratio, trim, and heave-to-beam ratio.

VALIDATION STUDY

To validate the numerical model, the hull was run at five speeds to compare the resistance, trim, and heave as functions of speed. The speeds simulated corresponded to length Froude numbers of 0.595, 0.893, 1.190, 1.488, and 1.785. The fine mesh from the mesh dependency study was used for all cases.

The results are compared here to the Fridsma [1] experiment, the theoretical prediction using the method developed by Savitsky [2], as well as the CFD work done by Mousaviraad et al. [8], Sukas et al. [9], and O'Shea et al. [7]. The cell counts in these previous CFD studies were 7.9 million, 7.5 million, and 514 million, respectively.

Compared to the experiment (Fig. 9), our (WSU) model over-predicted the resistance, under-predicted the trim, and under-predicted the heave for all speeds. However, the results matched the trends observed in the experiment, and the numerical deviations are acceptable from the engineering standpoint. The results of this model also matched reasonably well with the other CFD studies performed on this hull.

Sources of discrepancy can be related to the center of gravity (CG) locations. Mousaviraad et al. [8] observed that the CG position was critical for this hull, as small changes in the longitudinal CG could drastically influence the trim and resistance. They even used a shifted CG position to produce better fit to the test data.

Sukas et al. [9] were able to get good agreement with the experiment at higher speeds, but their trim at rest was different from that reported in the experiment, which suggests that either the CG position was different between the model and the experiment or some discrepancy in the model geometry was present.

It was observed in the Fridsma experiment [1] that placing a small piece of tape protruding from the hull chine helped alleviate the hull side wetting at higher speeds. This could also affect the numerical results. The present model tried to incorporate the small protrusion into model, but without knowing the exact geometry of the tape, the spray affects from the tape cannot be considered to be accurately modeled. The other CFD studies did not discuss this tape, and Mousaviraad et al. [8] mentioned the hull-side wetting occurring at sufficiently high $Fr = 1.19$, whereas our results showed no side wetting at this speed.

The Savitsky method provides a good indication for trim, but has large errors for resistance at lower speeds and does not capture the hump drag, whereas the CFD methods do. There are also very large errors in the heave at all speeds using the Savitsky method when compared to the CFD and experiment.

Overall, the present model with relatively coarse mesh accurately captured the hump speed, reasonably predicted drag, and approximately agreed with the previous CFD studies that employed much finer mesh. Hence, the present approach can be used to model planing hulls in the range of speeds from the displacement to planing regime.

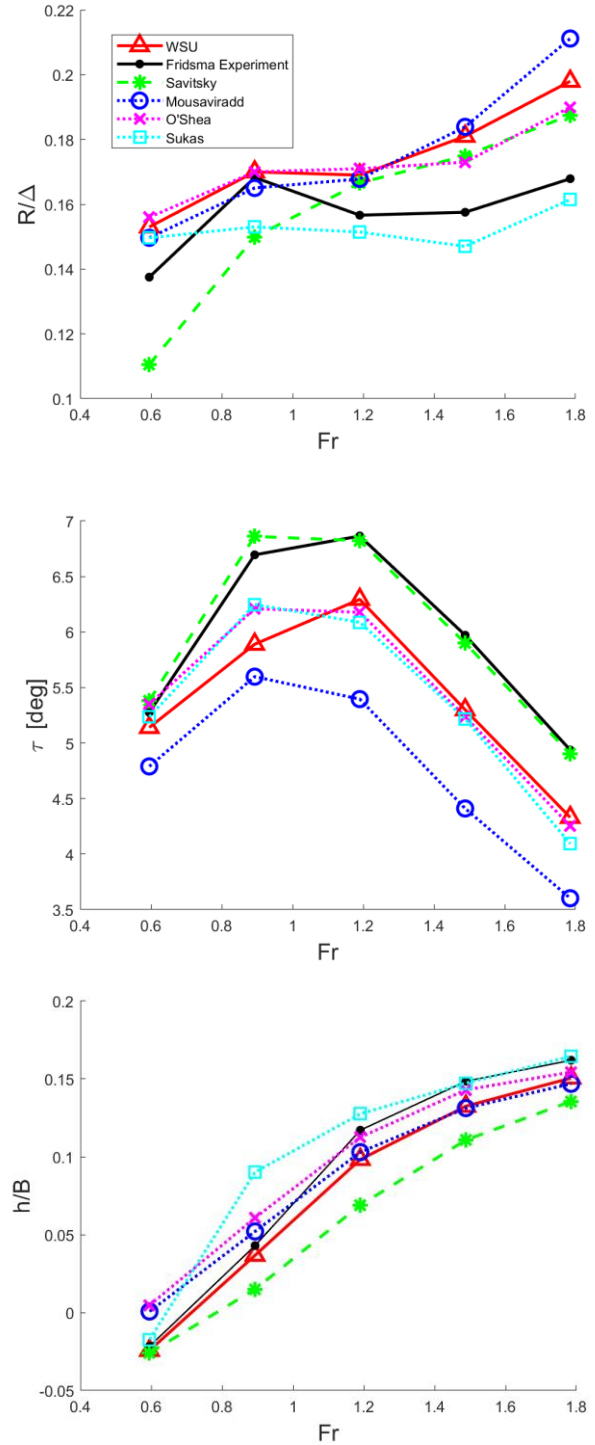


Fig. 9 Results for resistance, trim, and heave as functions of Froude number obtained from different studies.

Additional insight into planing hull hydrodynamics can be provided with illustrations of other water flow characteristics shown in Figs. 10-11. The piezometric pressure coefficient C_p is plotted on the hull bottom in Fig. 10. The piezometric

pressure is defined as having the hydrostatic pressure subtracted from the gage pressure. To non-dimensionalize this pressure, the result is then divided by the dynamic pressure to obtain the piezometric pressure coefficient. Therefore, this coefficient showcases only the dynamic effects of the pressure, and negates any influences caused by hydrostatics. When plotting C_p in Fig. 10, its minimum and maximum limits are chosen as -0.25 and $+0.5$, respectively, to highlight C_p variations on the entire hull surface. The extreme values of C_p can be outside the selected range in small zones at the water impingement zone and near the transom.

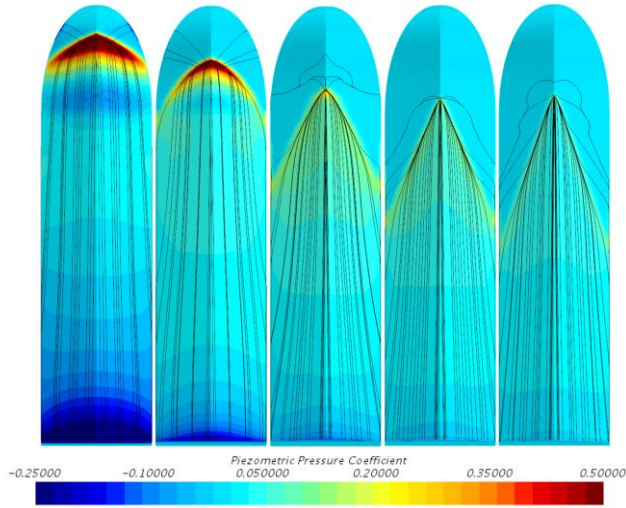


Fig. 10 Comparison of the piezometric pressure coefficient at different Froude numbers for the nominal hull. Hull speed increases from left to right.

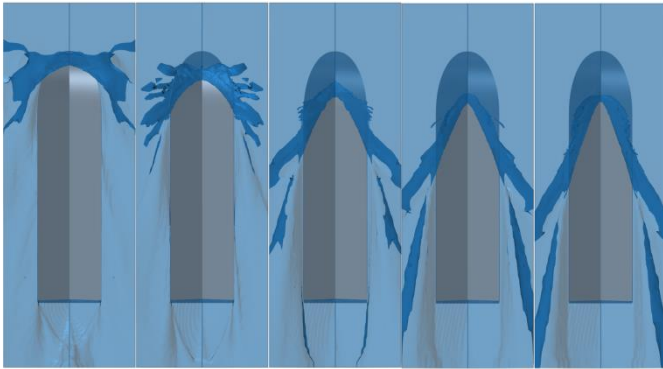


Fig. 11 Bottom views of the hulls at different Froude numbers. The grey hull surface is fully wetted, and the darker blue portions show areas of near-hull waves and spray. Hull speed increases from left to right.

The low piezometric pressures at the stern, noticeable at low speeds in Fig. 10, imply that flow is accelerating down the hull, whereas high pressure at the water impingement at the

bow illustrates a pronounced near-stagnation region. With increasing hull speed, zones with high absolute values of C_p decrease. In addition, the streamlines are overlaid on this figure (as thin black lines) to show how flow is moving along the hull.

An isosurface of the volume fraction of water equal to 0.5 with translucency was created to represent the free surface and is plotted in Fig. 11. This figure shows the fully wetted surface in grey, while also showcasing spray generated off the hull. It can be seen that at low speeds a part of non-prismatic bow is submerged, a significant bow wave is formed, and spray goes in various directions. In contrast, at planing speeds the spray is more aligned with the incident flow, and only the prismatic portion of the hull retains contact with water.

OVERLOADED HULL

In order to better understand hydrodynamics of overloaded planing hulls, we increased the weight of the hull discussed in the preceding section by 50% and re-ran the simulations to generate trim, heave, and resistance curves for the overloaded hull. The same numerical setup was used.

The hydrostatics between the two loadings were compared to make sure the overloaded hull was still reasonable from a hydrostatic point of view. The waterlines and hydrostatic resting positions can be seen in Fig. 12. The overloaded hull has a bit more bow rise at rest and sits deeper in the water, but is not drastically different from the nominal case while at rest.

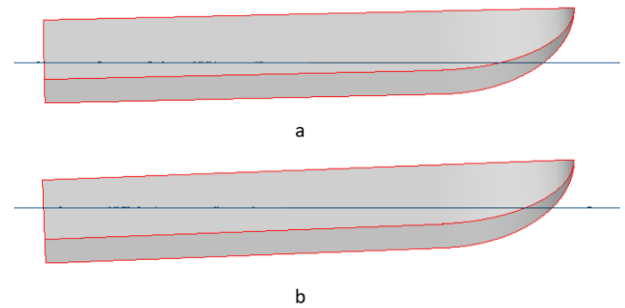


Fig. 12 Comparison of waterlines at hydrostatic condition. a) nominal hull b) overloaded hull

The hydrodynamic results for the nominal hull and overloaded hull are compared in Fig. 13. The nominal hull shows relatively flat resistance and trim curves in the considered speed range, whereas the overloaded hull has steeper resistance and trim curves, with both the resistance and trim increasing as hull velocity is increased.

It can be determined from the drag-weight ratio curve that the overloaded hull has smaller relative resistance compared to the nominal hull at the two lower length Froude numbers, since it still sails in the displacement or semi-displacement regimes, while the nominal hull shows a resemblance of the drag hump at $Fr \approx 0.9$. However, at higher speeds, the heavy hull resistance increases drastically, indicating a hump drag around the length Froude number of 1.5.

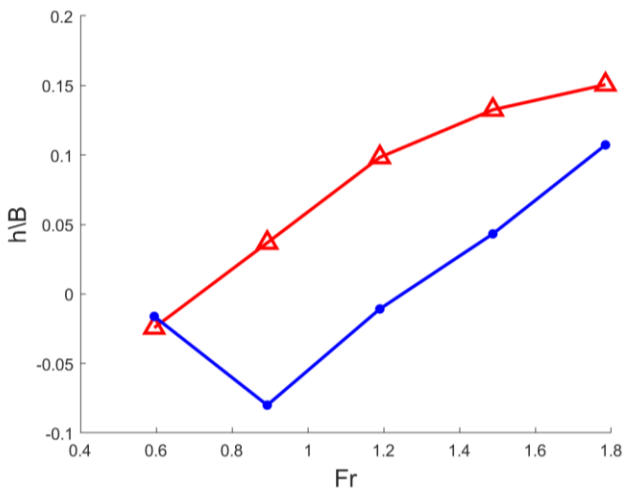
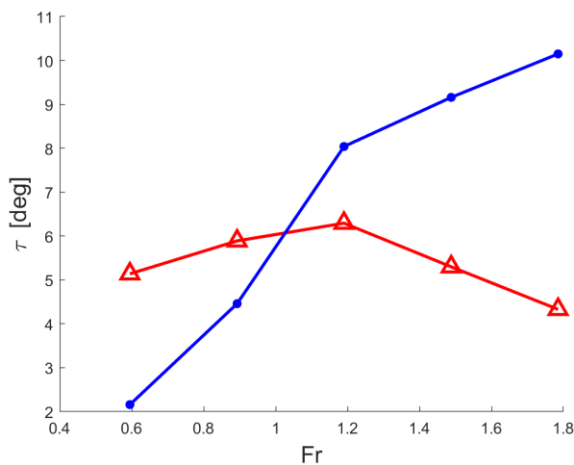
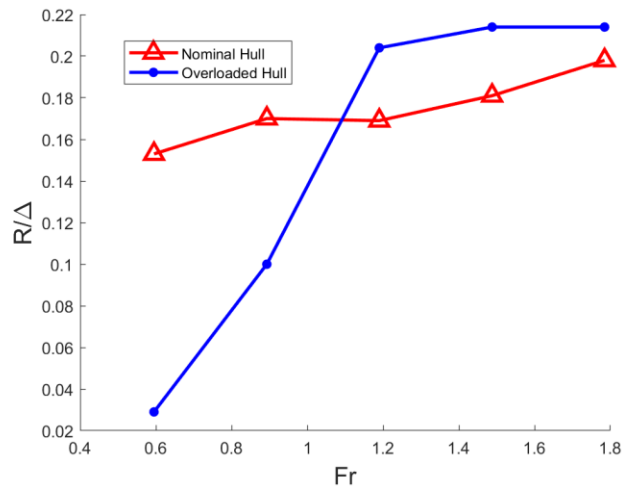


Fig. 13 Results for resistance, trim, and heave as functions of Froude number obtained for the nominal and overloaded hulls.

The resistance trend for the overloaded hull also correlates with the trim behavior. At lower speeds, more significant submergence of the curved bow shape results in the local pressure reduction behind the water impingement zone (Fig. 14), which is more pronounced than for a lighter hull (Fig. 10). This keeps the heavy hull more leveled and leads to smaller pressure drag and the resistance/weight ratio when compared to the nominal hull. At higher speeds, however, the overloaded hull produces a large bow wave (Fig. 15) and exhibits a high trim trying to climb on this wave. This consequently results in larger relative resistance (Fig. 13).

As for the heave, a drastic drop at $Fr \approx 0.9$ is seen in Fig. 13. This is caused by reduction of the piezometric pressure coefficient along the entire hull (Fig. 14), so the average bottom pressure is lower compared to the other speeds, which would tend to bring the heave downward.

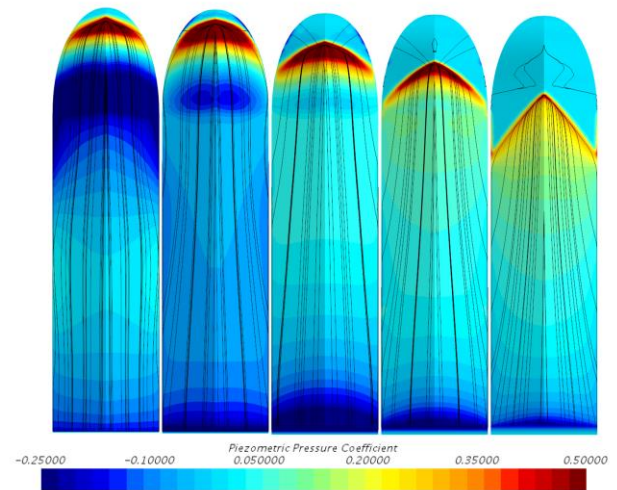


Fig. 14 Comparison of the piezometric pressure coefficient at different Froude numbers for the overloaded hull. Hull speed increases from left to right.

At the higher Froude numbers, the heavy hull has more violent spray formations in the bow region (Fig. 15), and the wetted surface includes a part of the curved bow, whereas this is not true with the nominal hull. The nominal hull's inception point of the free surface is clearly in the prismatic region of the hull (Fig. 11). On the heavy hull, the curved bow surface influences the flow the entire hull more so than in the nominal case. Compared to the nominal case, much higher pressures are also seen in the bow even at higher speeds, which leads to the increase in trim for the overloaded case.

It is not until the highest Froude number where it looks like the inception of the free surface is strictly in the prismatic portion of the hull (Fig. 15), and consequently this is where the resistance starts leveling off. Therefore, at most studied speeds the overloaded hull operates in the pre-planing regime despite high values (exceeding one) of the length Froude numbers.

We can mention one interesting but somewhat expected observation that a rough matching of the obtained curves of hydrodynamic characteristics, shown for two hulls in Fig. 13, can be achieved by shifting curves for the overloaded hull to the left (lower speeds) and downward. Then, the trends around the hump speeds ($Fr \approx 0.9$ for the light hull and $Fr \approx 1.5$ for the heavy hull) will look approximately similar for all presented parameters.

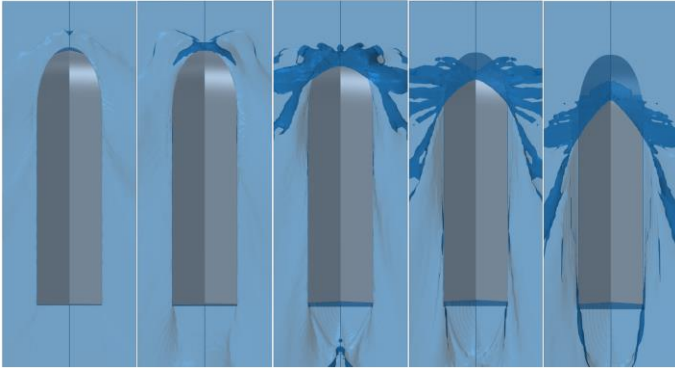


Fig. 15 Bottom views of the hulls at different Froude numbers for the overloaded hull. The grey hull surface is fully wetted, and the darker blue portions show areas of near-hull waves and spray. Hull speed increases from left to right.

CONCLUSIONS

In this study, a numerical model for a compact planing hull was validated and then compared to the same hull operating in an overloaded condition at the same speeds. At lower speeds, the heavy hull showed lower resistance values, since it was still sailing in the displacement regime. However, at higher speeds, the overloaded hull demonstrated higher resistance/weight ratios, associated with much higher trim near the new drag hump when compared to the lighter hull. From the economic considerations and/or due to thrust limitations, it is recommended that the overloaded hull should operate in the pre-hump regime.

Further studies, e.g., looking at different CG locations, may provide suggestions for improving characteristics of the overloaded hull at higher speeds. Investigations of more involved modifications of the hull geometry can be useful for planing hulls designed to perform in heavy loaded conditions at high speeds.

ACKNOWLEDGMENTS

This work was supported by ONR through Grant No. N00014-17-1-2553.

REFERENCES

[1] Fridsma, G., 1969, "A Systematic Study of the Rough-Water Performance of Planing Boats," Stevens Institute of Technology, Davidson Laboratory, Report No. 1275.

[2] Savitsky, D., 1964, "Hydrodynamic Design of Planing Hulls," *Mar. Technol.*, 1, pp. 71-95.

[3] Doctors, L.J., 1974, "Representation of Planing Surfaces by Finite Pressure Elements," 5th Australian Conference on Hydraulics and Fluid Mechanics, Christchurch, New Zealand.

[4] Wellicome, J.F. and Jahangeer, J.M., 1978, "The Prediction of Pressure Loads on Planing Hulls in Calm Water," *Trans. R. Inst. Naval Archit.*, 121, pp. 53-70.

[5] Matveev, K.I. and Bari, G.S., 2016, "Effect of Deadrise Angles on Hydrodynamic Performance of a Stepped Hull," *J. Engineering for the Maritime Environment*, 230(4), pp. 616-622.

[6] Bari, G.S. and Matveev, K.I., 2016, "Hydrodynamic Modeling of Planing Catamarans with Symmetric Hulls," *Ocean Eng.*, 115, pp. 60-66.

[7] O'Shea, T.T., Brucker, K.A., Wyatt, D., Dommermuth, D.G., Ward, J., Zhang, S., Weems, K., Lin, W.-M., Judge, C., and Engle, A., 2012, "Validation of Numerical Predictions of the Impact Forces and Hydrodynamics of a Deep-V Planing Hull," NSWCCD Report No. 50-TR-2012/040.

[8] Mousaviraad, S.M., Wang, Z., and Stern, F., 2015, "URANS Studies of Hydrodynamic Performance and Slamming Loads on High-Speed Planing Hulls in Calm Water and Waves for Deep and Shallow Conditions," *Applied Ocean Research*, 51, pp. 222-240.

[9] Sukas, O.F., Kinaci, O.K., Cakici, F., and Gokce, M.K., 2017, "Hydrodynamic Assessment of Planing Hulls Using Overset Grids," *Applied Ocean Research*, 65, pp. 35-46.

[10] A. De Marco, S. Mancini, S. Miranda, R. Scognamiglio, L. Vitiello, 2017, "Experimental and Numerical Hydrodynamic Analysis of a Stepped Planing Hull," *Applied Ocean Research*, 64, pp. 135-154.

[11] Frisk, D. and Tegehall, L., 2015, "Prediction of High-Speed Planing Hull Resistance and Running Attitude," Master's Thesis X-15/320, Chalmers University, Department of Shipping and Marine Technology.

[12] Xing, T. and Stern, F., 2010, "Factors of Safety for Richardson Extrapolation," *ASME Journal of Fluids Engineering*, Vol. 132, No. 6, 061403.